Research Article

ADVANCED PHOTONICS

Parallelization of frequency domain quantum gates: manipulation and distribution of frequency-entangled photon pairs generated by a 21 GHz silicon microresonator

Antoine Henry,[a,*] Dario A. Fioretto,[b] Lorenzo M. Procopio,[c] Stéphane Monfray,[d] Frédéric Boeuf,[d] Laurent Vivien,[b] Eric Cassan,[b] Carlos Alonzo-Ramos,[b] Kamel Bencheikh,[b] Isabelle Zaquine,[a] and Nadia Belabas[b,*]

[a]Institut Polytechnique de Paris, LTCI, Télécom Paris, Palaiseau, France
[b]Université Paris-Saclay, CNRS, Centre for Nanosciences and Nanotechnology, UMR 9001, Palaiseau, France
[c]Weizmann Institute of Science, Rehovot, Israel
[d]STMicroelectronics SAS, Crolles, France

Abstract. Harnessing the frequency dimension in integrated photonics offers key advantages in terms of scalability, noise resilience, parallelization, and compatibility with telecom multiplexing techniques. Integrated ring resonators have been used to generate frequency-entangled states through spontaneous four-wave mixing. However, state-of-the-art integrated resonators are limited by trade-offs among size, spectral separation, and efficient photon pair generation. We have developed silicon ring resonators with a footprint below 0.05 mm^2 providing more than 70 frequency channels separated by 21 GHz. We exploit the narrow frequency separation to parallelize and independently control 34 single qubit-gates with a single set of three off-the-shelf electro-optic devices. We fully characterize 17 frequency-bin maximally entangled qubit pairs by performing quantum state tomography. We demonstrate for the first time, we believe, a fully connected five-user quantum network in the frequency domain. These results are a step towards a generation of quantum circuits implemented with scalable silicon photonics technology, for applications in quantum computing and secure communications.

Keywords: integrated photonics; frequency domain; quantum gates; quantum networks.

Received Sep. 30, 2023; revised manuscript received Apr. 3, 2024; accepted for publication May 22, 2024; published online Jun. 28, 2024.

[DOI: 10.1117/1.AP.6.3.036003]

1 Introduction

Frequency encoding provides a resource-efficient way to access a high-dimensional Hilbert space within a single spatial mode, opening the way for scalable quantum information processing. This scheme has gained interest since 2017, when a universal scheme for quantum information with frequency-encoding was proposed.[1] Frequency-encoded entangled states are a major resource for quantum information and have since been generated in various nanophotonics structures, such as the Hydex microresonator (MR) (2017),[2] silicon nitride MRs (2018–2023),[3–5] lithium niobate waveguides,[4,6–8] and while frequency-entanglement can occur in any silicon-on-insulator (SOI) resonator generating photon pairs, it has only recently been observed on the SOI platform, combining SOI MRs.[9–11] The frequency bins are created by external filtering of the wideband nonlinear sources,[6–8,12] or by exploiting the inherently discrete frequencies of the resonators.[2,4,9,10]

SOI technology provides key advantages for the generation of correlated and entangled photon pairs, including the scalability and the availability of a wide library of high-performance optic and optoelectronic devices. Indeed, silicon photonics has been identified as an enabling technology for quantum

*Address all correspondence to Nadia Belabas, nadia.belabas@c2n.upsaclay.fr; Antoine Henry, antoine.henry@telecom-paris.fr

information.[13] In particular, it is possible to generate biphoton frequency combs through spontaneous four-wave mixing (SFWM) in high-quality-factor MRs.[14–17] SOI offers the ability to work in the telecom range, where photon pairs are produced by SFWM, and manipulated using available resources from classical optical telecommunications such as filters, demultiplexers and modulators, and available fiber networks. Moreover, in the telecom wavelength range, where the SOI is transparent and efficient for SFWM, off-the-shelf filters, demultiplexers, and modulators are available, and long-distance interaction between future quantum processors or communication nodes can be achieved using existing classical telecom infrastructures.

The manipulation of frequency bins separated by up to several hundreds of gigahertz can be made through nonlinear processes like optical frequency conversion.[18,19] However, this method may be hampered by limited configurability and by the optical noise from the pump required to generate the nonlinear phenomena. When generated at the telecom wavelengths, near 1550 nm, frequency bins can be manipulated using off-the-shelf telecom devices, such as electro-optic phase modulators (EOMs)[20–22] and programmable filters (PFs).[1,2,8,9] It has been shown that the combination of two EOMs and a PF allows arbitrary qubit transformation if the qubit mode spacing Δf is equal to the radio frequency Ω (RF) driving the EOMs.[23,24] The reconfigurability of such quantum frequency processors allows for various applications.[25–27]

The frequency mode spacing Δf is a key parameter. The limited bandwidth of standard telecom EOMs limits the maximum achievable qubit frequency spacing, Δf, to a few tens of gigahertz. In addition, low Δf boosts the spectral efficiency, i.e., maximizes the achievable Hilbert dimension for a given available source bandwidth. Yet, large resonators are difficult to fabricate, as propagation losses degrade the quality factor. Furthermore, SFWM efficiency scales inversely with Δf^2.[28] Achieving narrow frequency spacing with integrated resonators, while keeping high nonlinear efficiency, is a challenging task. Spectral separation of 40 to 50 GHz has been achieved using silicon nitride ring resonators with a radius near 500 μm, yielding a footprint exceeding 1 mm^2.[2–4] Frequency separation of only $\Delta f \approx 20$ GHz has been recently achieved by combining silicon rings with resonances separated by 200 GHz.[9,10] This clever design nevertheless gives rise to variable qubit mode spacing and limits the number of achievable frequency modes.

Frequency-entangled quantum states can be characterized by EOMs and PFs. A single modulator does not allow for a unitary control of a photonic qubit, but permits the quantum state tomography of high-dimensional states.[2–4,8–10] Quantum state tomography can be performed with parallelizable unitary operation on entangled qubits if the spacing is lower than the RF bandwidth. In Ref. 7, where frequency-entangled qubits are generated from a periodically poled lithium niobate spontaneous parametric down conversion (SPDC) source filtered by a fibered etalon frequency comb with a spacing of 25 GHz, quantum state tomography is performed with the [EOM–PF–EOM] configuration. The parallelization of two gates allows the control of two independent frequency qubits.

Quantum networks leverage the parallelization, i.e., independent control of qubits, together with wavelength demultiplexing to create networks of connected users.[29–32] By distributing frequency-correlated two-photon entangled qubit pairs generated by a single-photon pair source, it is possible to generate complex networks up to trusted-node-free, fully connected networks.[33–36] In contrast with networks that rely on trusted nodes, point-to-point connections or active switching,[29,30,37] trusted-node-free, fully connected networks are a scalable way to create a quantum network connecting a large number of users.[38]

In this paper, we report the parallelization of 34 tunable electro-optic frequency domain quantum gates, implemented with a single [EOM–PF–EOM] configuration. We develop to this end an SOI spiral ring resonator with a footprint below 0.05 mm^2 and a frequency channel separation $\Delta f = 21$ GHz. The rings are fabricated using STMicroelectronics' silicon photonics R&D and manufacturing platform based on 300-mm SOI wafers and 193-nm-deep-ultraviolet (DUV) lithography, ensuring compatibility with large-scale production.[39] The narrow spectral separation allows photon pair generation through SFWM on more than 70 frequency modes over a 1.4 THz bandwidth. In addition, the 21 GHz spectral separation allows implementing parallel and arbitrary qubit transformations, based on the [EOM–PF–EOM] scheme implemented with commercially available electro-optic devices. We perform quantum state tomography on frequency domain maximally entangled photons. We select 20 correlated frequency modes to encode 10 frequency-entangled photon pairs to create a trusted-node-free fully connected network where five users each share a secure key with every other user.

2 Results

2.1 21 GHz SOI Spiral MR

We generate photon pairs through SFWM in an SOI MR. The integrated photonic devices were fabricated using STMicroelectronics' silicon photonics R&D and manufacturing platform based on 300 mm SOI wafers. The structures were defined with DUV lithography and transferred to the silicon layer with reactive ion etching.[39] A 2 mm-thick PMMA layer was deposited over the chip surface for protection. The thickness of the guiding silicon layer is 300 nm, for compatibility with STMicroelectronics' silicon photonics R&D and manufacturing platform. In Fig. 1(a), we show the dispersion calculated as a function of the wavelength for different waveguide widths. We find that a waveguide width of 700 nm yields small anomalous dispersion near 1550 nm. The spiral waveguide length is set to 3.54 mm to yield a free spectral range (FSR) near 21 GHz, which determines the frequency channel separation (Δf). The spiral shape is chosen to reduce the footprint of the device. This reduced layout has a negligible effect on the waveguide dispersion, and thus on the phase-matching conditions and the bandwidth of the generated biphoton comb. The waveguide bendings follow a Bezier trajectory to minimize transition mismatch between straight and curved waveguides, ensuring a smooth transition between the straight and bent waveguides, with a bend radius that is reduced adiabatically.[40,41] Even if this approach is known to minimize transition mismatch, there is a residual loss penalty compared to a circular resonator of a larger footprint, which will slightly reduce the optical quality factor. Still, as shown in Figs. 1(c) and 1(d), the proposed resonator exhibits a full width at half-maximum of 450 MHz, leading to a quality factor $Q \approx 4.75 \times 10^5$. These results compare favorably with previously reported silicon resonators used for photon-pair generation,[42,43] while achieving an FSR of only 21.18 GHz. Note that the area of our resonator, of mm^2 (165 μm by 255 μm) is 23 times smaller

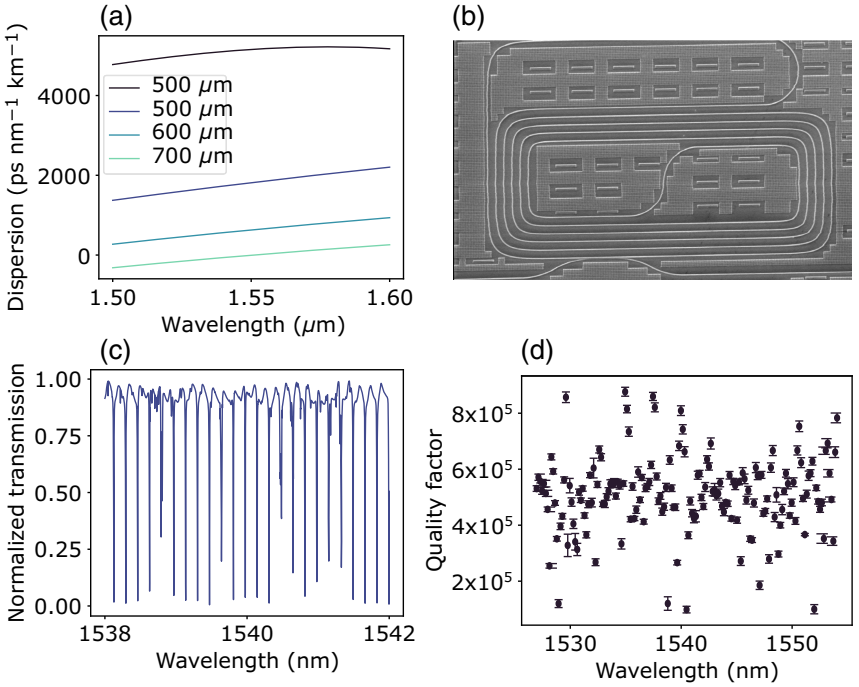

Fig. 1 (a) Waveguide dispersion as a function of the wavelength, calculated for a waveguide height of 300 nm and different waveguide widths. (b) SEM image of the resonator. (c) Normalized transmission spectrum of the resonator. (d) Measured quality factor as a function of the wavelength.

than that of a circular ring resonator with the same length. The sample temperature is tuned and stabilized by a Peltier module at 25°C ± 0.01°C. Cleaved SMF28 fibers, set at a 15 deg incidence angle, are used to couple light in and out of the chip, through single-etch grating couplers. The measured fiber-to-fiber insertion loss is 7.6 dB, i.e., 3.8 dB per coupler including propagation loss.

For a broadband photon pair generation process, the FSR needs to be constant as a function of the optical wavelength. Figure 2 shows the evolution of the FSR as a function of the wavelength and optical frequency. We observe a flat FSR throughout the working wavelength range.

The photon pairs are generated through SFWM. An optical pump of frequency ω_p is tuned on a resonator mode so that signal and idler photons are emitted on symmetric resonances at frequency $\frac{\omega_p}{2\pi} \pm n \cdot \mathrm{FSR}$ ($n \in \mathbb{N}$). As a result, the measured FSR varies less than 20 MHz over the whole measured SFWM spectrum where the correlated pairs can be observed from 1526.7 to 1553 nm. The quantum state $|\phi\rangle$ of the generated photon pairs is expressed as

$$|\phi\rangle = \frac{1}{\sqrt{N}} \sum_{n=1}^{N} e^{i\alpha_n} |I_n\rangle |S_n\rangle, \tag{1}$$

where I_n and S_n stand for idler and signal frequencies with $I_n = \frac{\omega_p}{2\pi} - n \cdot \mathrm{FSR}$ and $S_n = \frac{\omega_p}{2\pi} + n \cdot \mathrm{FSR}$, respectively. α_n corresponds to the biphoton residual spectral phase,[4] within the 450 MHz linewidth of the resonances. The ring resonator intrinsically produces frequency-bin entangled qudits of dimension N where N is limited here by the bandwidth of the PFs (5 THz) and phase-matching conditions.

To characterize the spectral correlations, we measure the anti-diagonal terms of the joint spectral intensity (JSI) of the biphoton state. We use the setup shown in Fig. 3(a). A bandpass (BP) filter is used to suppress the amplified spontaneous emission of the CW pump laser at 1540 nm up to 40 dB. Two fibered notch Bragg filters with a bandwidth of 80 GHz are used at the output of the SOI MR to filter out 70 dB of the laser light, and an additional filtering of the laser light is done with the PF (Finisar WaveShaper 4000A), ensuring more than 100 dB pump rejection. The spectrally correlated photon pairs are spatially separated by the same PF, sent to superconducting nanowire single photon detectors (SNSPDs) with a 70% quantum efficiency, and analyzed using the Swabian TimeTagger Ultra (TT). In this paper, the coincidences are taken in a 1 ns window. The dead time of the detectors is ≈20 ns, allowing maximum efficiency for the range of count rates observed in this work (in the order of

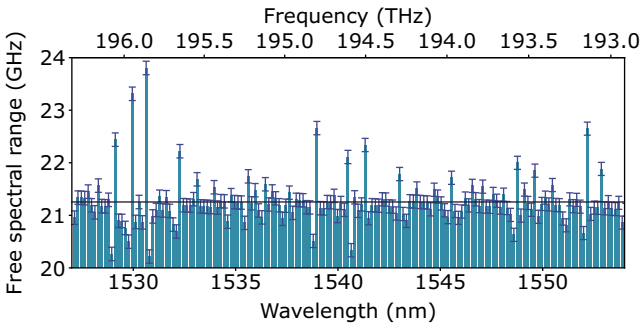

Fig. 2 Measured FSR as a function of wavelength and optical frequency around 1540 nm.

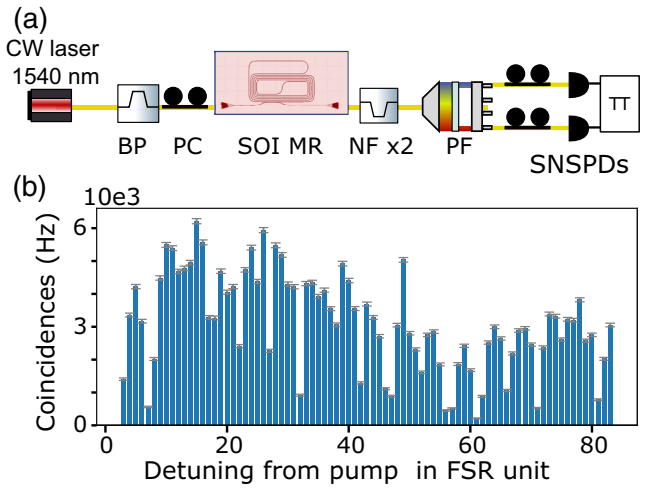

Fig. 3 (a) Setup for measurement of the joint spectral intensity. BP, bandpass filter; NF, notch filter; PF, programmable filter; PC, polarization controller; and SNSPDs, superconducting single-photon detectors. (b) Anti-diagonal elements of the JSI measurement for every accessible signal-idler pair from $n = 3$ to $n = 83$.

40 kHz). The combined time jitter of the SNSPDs and the TT is around 120 ps. Consistently generating photon pairs, requires stabilization due to the small cavity linewidth. We perform thermal stabilization using a Peltier module and also stabilize the frequency of the optical pump. As we observe a decrease in transmission through the device when tuning on a cavity mode, we utilize the pump's output intensity as feedback to shift the pump's frequency to a point where the intensity is at a minimum. Placing the optical pump at ± 500 MHz from the cavity mode allows for automatic tuning. The 100 ms response time ensures a fast stabilization throughout the experiment.

In Fig. 3(b), we plot the number of coincidences between correlated signal and idler photons as a function of the selected resonance number n associated with the frequency pairs I_n, S_n.

The off-diagonal terms, not shown here, are at the level of accidental coincidences of $\approx$200 coincidences per second. The low FSR of our resonator allows access to a larger number of resonances compared to previous works,[2–4] providing possibilities of parallelization of operations over a larger number of qubits and perspectives for the processing of higher-dimensional quantum states. The long cavity nonetheless leads to more propagation losses. The overall decrease of the coincidences with increasing n is linked to the spectral transmission of the grating couplers.

For a specific signal idler pair, $|S_{15}, I_{15}\rangle$, we give single counts, two-photon coincidences between the signal and idler photons, as well as the three-photon coincidences between a signal and an idler whose path is split in two by a beam splitter. We infer from these measurements the generated number of pairs, the coincidence-to-accidental ratio (CAR), and the heralded $g^{(2)}(0)$. The generated number of pairs is calculated using the ratio between the product of the single counts and coincidence counts $N_P = \frac{N_I \times N_S}{N_C}$, the CAR is obtained by computing the ratio between actual and accidental two-photon coincidences,[44] and the $g^{(2)}(0)$ is computed using the three-photon coincidences. Figure 4(a) shows the setup of the experiment. The two photons are deterministically separated using a PF that routes the modes $|S_{15}\rangle$ and $|I_{15}\rangle$ to distinct fibers. The signal photon is directly routed to an SNSPD. In contrast, the idler photon either goes directly to the detector or goes through a fibered beam splitter whose outputs are directed to two single-photon detectors. Figures 4(b)–4(f) show, respectively,

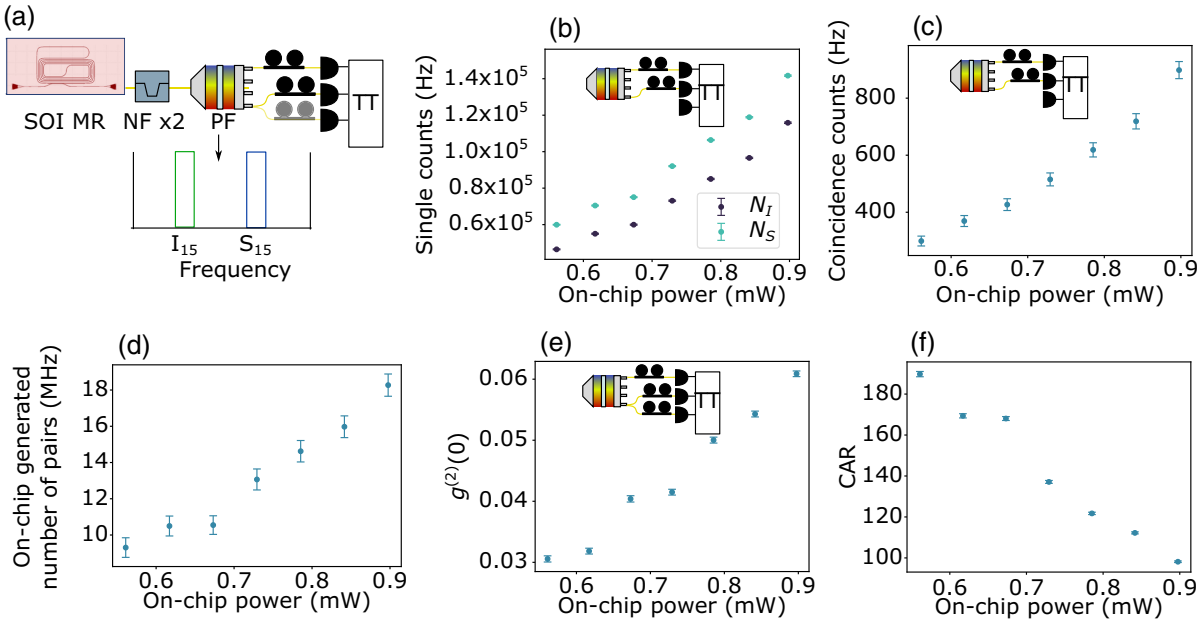

Fig. 4 Photon pair generation and heralded single-photon characterization of the SOI MR. (a) Setup for measuring single counts, two-photon coincidences, and three-photon coincidences. NF, notch filter; PF, programmable filter; and TT, time tagger. (b) Single counts, (c) coincidences, (d) generated number of pairs, (e) heralded $g^{(2)}(0)$, and (f) CAR, each as a function of input power (refer to text).

the measured single counts, the coincidence rate, the generated number of pairs, $g^{(2)}(0)$, and the CAR as a function of the on-chip power.

The performance of our source can be compared to the literature by computing the internal brightness B, corresponding to the number of pairs normalized by the on-chip power and spectral bandwidth. Table 1 compares several values of brightness for similar works with silicon MRs. We assess a high value of brightness, which correlates with the measured high quality factors.

2.2 Frequency-Domain Quantum State Tomography

In this section, we demonstrate quantum state tomography of a frequency two-dimensional maximally entangled state produced by our 21 GHz SOI MR. A first PF1 (see Fig. 5) selects two adjacent signal and idler mode pairs from the high-dimensional two-photon state of Eq. (1) coming out of the resonator to produce the biphoton maximally entangled state $\frac{1}{\sqrt{2}}(|I_n S_n\rangle + |I_{n+1} S_{n+1}\rangle)$.

To perform the tomography of this state, single qubit rotations in the frequency domain are necessary. We implement those using EOMs and PFs as demonstrated in Ref. 24 (see Appendix A). The setup is shown in Fig. 5 and uses these devices sequentially in an [EOM–PF–EOM] configuration. RF driving of the EOM at $\Omega = \mathrm{FSR}$ is possible here because the low FSR of our MR is compatible with the 40 GHz bandwidth of the EOM. With this configuration, the [EOM–PF–EOM] device shown in Fig. 5 can achieve parallel independent manipulation of signal and idler photons.

Figure 5 shows a simplified setup for the quantum state tomography. In the full setup, polarizers are present before each EOM. Before each detector, a polarizer is also added to control the input polarization and a fibered notch filter around 900 nm is placed to suppress parasitic calibration light coming from the PF.

Previously reported tomography in the spectral domain used a single EOM.[2–4,9] Such a simple setup can be used when the frequency spacing between two modes is too large to match the RF driving frequency Ω and then corresponds to a multiple of Ω. This setup has the advantage of low loss but does not allow independent unitary operations on parallel qubits. In Ref. 7, quantum state tomography was performed using two parallel tunable quantum gates with the same [EOM–PF–EOM] configuration. A Bayesian method based on measurements only in the $\mathbb{Z}$ and $\mathbb{X}$ bases was used to reconstruct the density matrix,

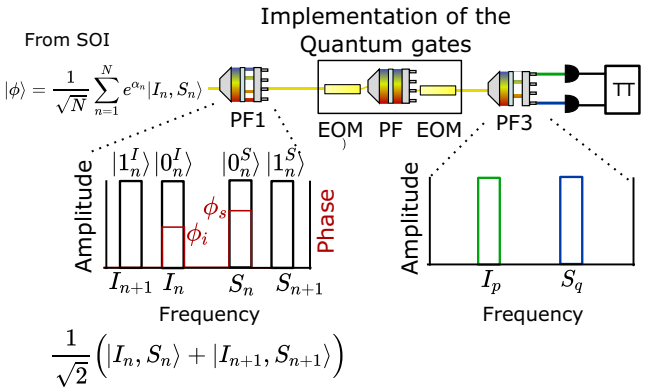

Fig. 5 Setup for the quantum state tomography. PF, programmable filter; EOM, electro-optic phase modulator. Insets are the action of the PFs on the frequency modes. PF1 is used both as an amplitude filter to select the four modes of the two qubits, and as a phase gate implementing a phase ϕ_i and ϕ_s on the frequency modes I_n and S_n. The boxed devices implement identity or Hadamard gate on the qubits. All the projections required for the tomography are accessible with these two gates. PF3 selects two modes I_p and S_q, where $p, q \in \{n, n+1\}$.

and a fidelity of 0.92 ± 0.01 to a $|\Psi^+\rangle$ entangled state was obtained.

Our logical qubits are defined as follows: $|0_n^X\rangle = |X_n\rangle$ and $|1_n^X\rangle = |X_{n+1}\rangle$, where $X = S, I$ refers to the logical signal or idler qubit (see Fig. 5). To perform the quantum state tomography, we need to project the two qubits onto four state vectors belonging to three different bases $\mathbb{Z} = \{|0_n^X\rangle, |1_n^X\rangle\}$, $\mathbb{X} = \{|+_n^X\rangle, |-_n^X\rangle\}$, and $\mathbb{Y} = \{|+i_n^X\rangle, |-i_n^X\rangle\}$, where $|\pm_n^X\rangle = \frac{1}{\sqrt{2}}(|0_n^X\rangle \pm |1_n^X\rangle)$ and $|\pm i_n^X\rangle = \frac{1}{\sqrt{2}}(|0_n^X\rangle \pm i|1_n^X\rangle)$. The quantum gate (see Fig. 5) allows us to choose between the $\mathbb{Z}$ and $\mathbb{X}$ bases. To access the $\mathbb{Y}$ basis, we use PF1 to apply a relative phase shift ϕ_i (ϕ_s) between the modes of the idler (signal) qubit. $C_{a,b}$ denotes the coincidence numbers corresponding to the projections on vectors $|a\rangle$ and $|b\rangle$ from the three different bases $\mathbb{X}$, $\mathbb{Y}$, and $\mathbb{Z}$. Table 2 shows the recorded coincidences for the 16 projections performed on the two-qubit state for $n = 34$.

Figure 6 shows the reconstructed density matrix. Comparing it to the density matrix of a maximally entangled state $|\phi^+\rangle = \frac{1}{\sqrt{2}}(|I_{34}, S_{34}\rangle + |I_{35}, S_{35}\rangle)$, we obtain a fidelity $\mathcal{F} = 0.961 \pm 0.007$. The errors are calculated using Monte Carlo methods.

Table 1 Comparison of internal brightness, FSR, and frequency channels accessible with commercial EOMs and other SOI implementations. We measured the brightness B on the signal-idler pair $|I_{15}, S_{15}\rangle$. *: Clementi et al.[9] and Borghi et al.[10] used several coupled rings to achieve, respectively, an effective 18 GHz and a 15 GHz mode spacing.

Work	B (pairs s^{-1} mW^{-2} GHz^{-1})	Q	FSR (GHz)	Number of frequency channels
Oser et al.[43]	5×10^5	3×10^4	200	—
Mazeas et al.[42]	1.6×10^6	4×10^4	230	—
Jiang et al.[45]	6.24×10^7	$3.47 \times 10^5 / 4.94 \times 10^5$	2315	—
Clementi et al.[9]	4.80×10^7	1.5×10^5	*	Two signal-idler pairs
Borghi et al.[10]	$1.80 \times 10^5 / 2.50 \times 10^5$	$5.7 \times 10^4 / 7.8 \times 10^4$	*	Four signal-idler pairs
This work	$(5.1 \pm 3) \times 10^7$	4.75×10^5	21	80 signal-idler pairs

Table 2 Coincidences for the two-photon projections $C_{a,b}$ integrated for 125 s, in a coincidence window of 1 ns.

Projections	Coincidences	Projections	Coincidences
$C_{0,0}$	1548	$C_{+,0}$	716
$C_{0,1}$	36	$C_{+,1}$	767
$C_{0,+}$	622	$C_{+,+}$	1275
$C_{0,+i}$	663	$C_{+,+i}$	608
$C_{1,0}$	22	$C_{+i,0}$	837
$C_{1,1}$	1553	$C_{+i,1}$	695
$C_{1,+}$	692	$C_{+i,+}$	723
$C_{1,+i}$	664	$C_{+i,+i}$	42

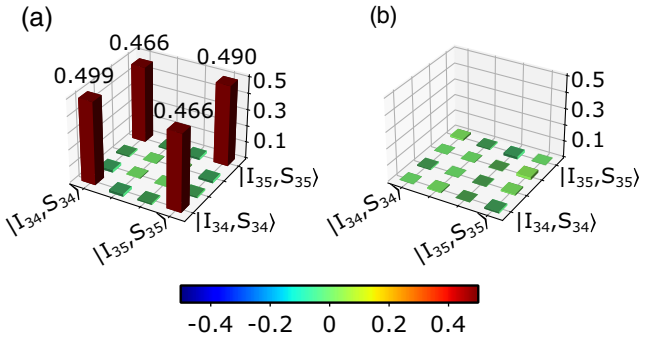

Fig. 6 Numerical reconstruction of the experimental density matrix of a two-qubit frequency-bin entangled state generated by the SOI resonator + PF1. (a) Real part and (b) imaginary part.

Having checked the fidelity of the produced frequency-entangled state, we take advantage of the broad bandwidth of our source and the versatility of the [EOM–PF–EOM] setup to parallelize the measurement of such high-quality entangled states by performing 34 quantum gates on 17 frequency-entangled qubit pairs, in a first implementation of frequency-encoded quantum communication protocol.

2.3 *Frequency-Bin Entangled Photons in a Fully Connected Trusted-Node-Free Network*

Quantum key distribution is one of the most mature applications of quantum information. Beyond original protocols involving only two parties, current efforts push towards multi-user quantum networks.[31] Trusted-node architectures allow for the creation of such networks but require users to trust part of the network. Quantum networks based on the demultiplexing of spectrally correlated entangled states enable scalable multi-user quantum networks.[33,35,36] In this section, we show a proof of principle of a trusted-node-free fully connected network of up to five users in which every user can share a secure key with every other user, using frequency-bin entangled qubits generated by our broadband photon pair source. In previous implementations or proof-of-principle experiments based on time-bin or polarization-based entangled sources,[33–35,46] the main challenge was phase or polarization stabilization. In addition to the previously mentioned assets, the frequency degree of freedom that we harness here has the advantage of requiring no phase stabilization for superposition analysis.

In this setup, polarization control is nevertheless necessary when entering the modulators. Recent advances have proposed schemes using polarization diversity EOMs to address this challenge,[47] which is a relevant and additional asset for real-world applications. As we encode frequency qubits on distinct pairs of adjacent frequencies, we can use a PF as a demultiplexer to spectrally separate and distribute the pairs to respective users to create a network. For each mode pair, compensation for the biphoton residual phase is required in order to produce the desired $|\phi^+\rangle$ states.[4]

To validate our scheme, we first show that the parallelization of the quantum gate enables measurement of entanglement for qubits separated by two guard modes, allowing for a measured cross talk $\leq 10^{-3}$ between adjacent quantum gates (see Appendix A). Figure 7 shows the fidelity for the accessible frequency-bin entangled pairs. We start from the $n = 10$ resonance from the pump frequency, to avoid any residual pump laser leakage. The fidelity is higher than 0.8 for 14 pairs. The few lower values are related to the dips observed in the coincidence spectrum shown in Fig. 3 around the 50th and 70th resonances from the pump.

Important metrics for quantum networks are the key rate and qubit error rate (QBER). We deduce these parameters from our coincidence measurements, using the method proposed in Ref. 48. We use the coincidences in the $\mathbb{Z}$ basis ($C_{0,0}$, $C_{0,1}$, $C_{1,0}$, $C_{1,1}$) and the $\mathbb{X}$ basis ($C_{+,+}$, $C_{+,-}$, $C_{-,+}$, $C_{-,-}$) to compute the raw coincidence rate, QBER, and sifted key rate (see Appendix B).

Figure 8(a) shows, for each accessible pair, the number of raw coincidences R_{raw} and the QBER. By comparing it with Fig. 7, we see that, as expected, the qubits with a lower raw key rate (and higher QBER) are also the ones with the lower fidelity to an entangled state. A given pair achieves secure quantum communication only if the corresponding QBER is lower than the positive key rate threshold of 0.11.[49] Among the 17 accessible pairs, only 12 satisfy this condition. A sifted

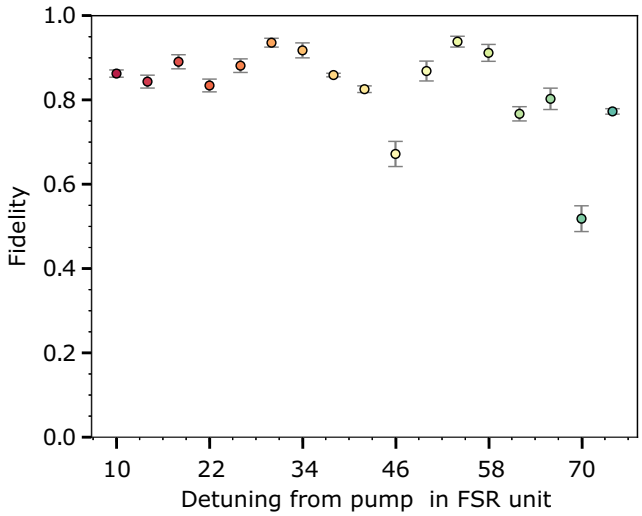

Fig. 7 Fidelity to a maximally entangled state for several frequency-bin entangled photon pairs. The *x*-axis corresponds to the number of resonances between the frequency qubit and the pump mode.

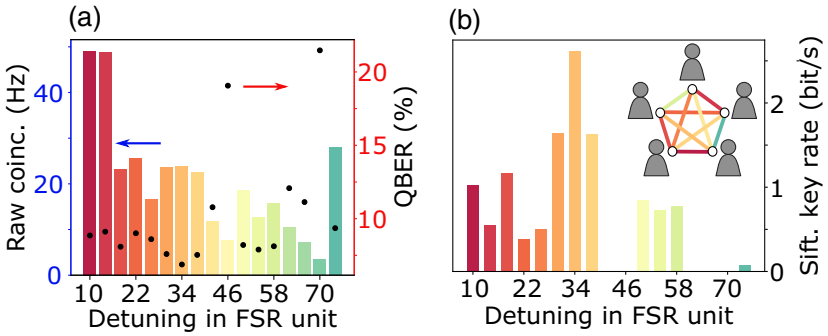

Fig. 8 (a) Raw coincidences (bars) and QBER (dots) between two users and (b) sifted key rate, calculated using the method in Ref. 34 as a function of n, spectral detuning from the pump. Each link between two users is a two-qubit frequency-bin entangled pair and is color-coded. For example, the bottom users of the network in the inset of (b) receive, respectively, the two frequency channels $|I_{10}\rangle$, $|I_{11}\rangle$ and $|S_{10}\rangle$, $|S_{11}\rangle$, which connect them in the network.

key rate in bit/s can also be derived from the raw rate R_{raw} using the method in Ref. 34, as depicted in Fig. 8(b). The inset in Fig. 8(b) shows how the distribution of 10 photon pairs is used to create a node-free quantum network of five users.

In this proof-of-principle experiment, the achieved key rates (0.5 to 2.5 bits/s) are limited by the performance of the source, as well as the insertion loss of the devices (14 dB for the three PFs and the two EOMs). As an example, reducing the insertion loss of each device to 1 dB per device would increase the sifted key rate to 50 bits/s. Integrating these components on the same chip would help to limit losses and improve the overall insertion loss of the [EOM–PF–EOM] configuration to 1.3 dB.[50] Several methods are proposed to achieve the integration of elements allowing the manipulation of frequency-bin qubits.[51,52] It is also worth noting that the number of accessible pairs could be increased by setting the pump frequency at the center of the PF bandwidth.

3 Conclusion

In this paper, we introduce an SOI MR for producing photon pairs at telecom wavelengths through SFWM and encoding frequency-bin qubits on adjacent pairs of resonances. Due to the broadband emission of the source and the 21 GHz FSR, we can generate up to 17 pairs of frequency-entangled qubits. We manipulate these qubits using quantum gates based on a single set of devices composed of one PF between two EOMs, enabling independent control of each qubit. This leverages the ability to use these reprogrammable quantum gates for quantum information applications.

We demonstrate quantum state tomography with these quantum gates on parallel qubits and assess fidelity to a $|\phi^+\rangle$ entangled state of over 0.8 for 14 of them.

Finally, we demonstrate a local proof of concept of a fully connected network and compute the key rate and QBER of 17 photon pairs, taking into account the threshold for attacks on the quantum channels and error correction. We can distribute 10 photon pairs and create a fully connected network of up to five users.

Scaling up the dimensionality of the manipulated quantum states is an intrinsic feature of frequency encoding. Arbitrary manipulation of higher-dimensional states would require no additional optical elements. Summing $N-1$ RF harmonics to drive the EOMs would enable the manipulation of N-dimensional entangled states with the [EOM–PF–EOM] configuration. An alternative approach with the same [EOM–PF–EOM] configuration and a single tone, or with one EOM enables qutrits manipulation.[2,3,6,8–12] However, this approach cannot independently implement arbitrary quantum gates to parallel qutrits. Moreover, on-chip integration of electro-optic devices and PFs is a promising lead to reduce the losses (currently around 9.5 dB for our quantum gates implementation).[50] SOI is a platform of choice for these integration purposes, as it allows for hybrid integration of lithium niobate with silicon photonics,[53,54] thus high speed EOM on chip.[55] Integration of frequency-domain transformations has also been proposed using a lithium niobate resonator driven by RF signals.[51,52] Our work thus offers perspectives for scalable frequency-domain architectures for high-dimensional and resource-efficient quantum communications.

4 Appendix A: Frequency-Domain Quantum Gates

4.1 Gate Characterization

In this section, we use a combination of EOMs and PFs to create frequency-bin quantum gates[23,24] that can be parallelized to a large number of qubits. The setup in Fig. 9(a) presents the quantum gate, composed of two EOMs iXblue MPZ-ln-40 (EOM1 and EOM2), driven by a multichannel RF sine wave generator Anapico APMS33G, and one phase-only programmable filter Finisar WaveShaper 1000A (PF). The overall insertion loss of the quantum gate is around 9.5 dB from the input of the first modulator to the output of the second. The time-dependent phase shift $\phi(t)$ applied by the EOM to the optical wave is proportional to the sine wave produced by the RF generator,

$$\phi(t) = \mu \cos(\Omega t + \theta), \tag{2}$$

where the RF frequency Ω determines the mode separation between the generated frequency modes $|\omega_n\rangle = |\omega_0 + n\Omega\rangle$, and μ is the modulation index, proportional to the RF voltage V: $\mu = \pi \frac{V}{V_\pi}$. V_π is the voltage giving rise to a π phase shift. The specific settings of the modulators and PF allowing the implementation of the quantum gate (tomography) are the following: both modulators must be driven with the modulation index $\mu = 0.81$ and the relative phase between them must be set to π.

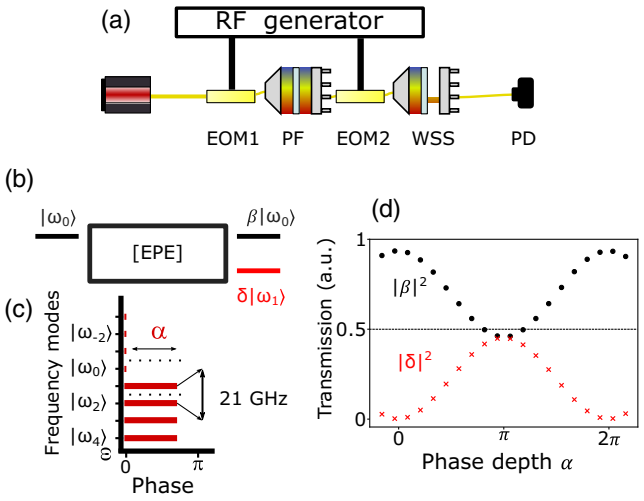

Fig. 9 Classical characterization of the quantum gate. (a) Principle of a frequency-domain operation. (b) Principle of a frequency-domain quantum gate. (c) Phase pattern applied by the PF. (d) Measured tunability of the quantum gate operation.

This operation is achieved by using the multichannel available on the generator, on which we can set a relative phase, ranging from 0 to π. It is noteworthy that compensation of the dispersion is required in order to keep this relative RF phase shift constant at all optical frequencies within the PF bandwidth. Another PF is used as a wavelength-selecting switch after the quantum gate to select the frequency mode to be detected by the IR photodiode. Figure 9(b) shows the principle of the operation performed. We define a frequency-bin qubit as a qubit for which the information is encoded on two frequency modes, here generically called $|\omega_0\rangle$ and $|\omega_1\rangle$. The goal of the quantum gate is to apply a controlled rotation on the qubit, here represented by the coefficients β and δ. To characterize the quantum operation, we use the fidelity $\mathcal{F}$ and the success probability $\mathcal{P}$[23],

$$\mathcal{F} = \frac{\mathrm{Tr}(W^\dagger T)\mathrm{Tr}(T^\dagger W)}{\mathrm{Tr}(W^\dagger W)\mathrm{Tr}(T^\dagger T)}, \quad \mathcal{P} = \frac{\mathrm{Tr}(W^\dagger W)}{\mathrm{Tr}(T^\dagger T)}, \tag{3}$$

where the fidelity corresponds to how close the realized operation (W) is to the ideal case (T), and the success probability measures the unitarity of the operation, accounting for the energy loss toward unwanted frequency modes.

Figure 9(c) represents the phase pattern applied by the PF to tune the operation of the gate. A step phase of height α is applied between the two qubit modes. In order to characterize the spectral processing implemented by this single-qubit gate, we use coherent light, as it is sufficient to characterize a single-qubit gate.

Figure 9(d) shows the effect of the phase difference α applied by the PF between the two qubit modes on the quantum gate, evolving from identity ($\alpha = 0$) to Hadamard operation ($\alpha = \pi$). The success probability experimentally reaches $\mathcal{P} = 0.95$, implying that the intrinsic transmission of the quantum gate is slightly below 0.5 but the splitting between the two modes is balanced, leading to a fidelity $\mathcal{F} = 0.99$. The success probability does not take into account the insertion loss of each device, summing up to around 9.5 dB (3.5 for the PF, and 3 for each modulator).

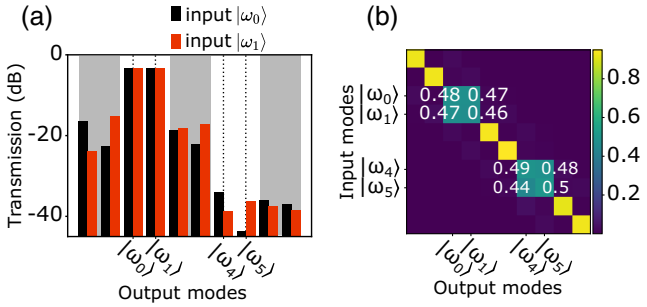

Fig. 10 (a) Light coupling from mode $|\omega_0\rangle$ (black) or $|\omega_1\rangle$ (red) into nine neighboring modes. The gray shaded areas represent the guard modes that are not used for parallelization. (b) Transmission measurement for nine frequency modes when a Hadamard gate is applied to two qubits separated by two guard modes.

4.2 Gate Parallelization

In these experiments, the mode spacing is taken to be 21 GHz. This is compliant with the resolution of the PFs (10 GHz), and the accessible modulation bandwidth of commercial EOMs (40 GHz). The phase pattern depicted in Fig. 9(c) shows a step phase applied between the two modes of the qubit. By applying a phase change over several pairs of frequency modes, it is possible to parallelize independent quantum operations over several frequency-bin qubits.

It is important, for parallelization, that two consecutive gates are isolated from each other. To determine what is the minimum desired spacing between each qubit, we send light through the quantum gate, tuned to realize the Hadamard transformation. We define the cross talk between the qubit as the portion of the light being converted from one qubit to another. The experimental results are shown in Fig. 10(a), where the black (red) lines correspond to the measured light when we input light in the mode ω_0 (ω_1). From this figure, we see that two separation modes between consecutive operations are enough to ensure less than 10^{-3} cross talk between two qubits. Figure 10(b) shows the intensity transmission matrix of a 10-dimensional frequency space, where we apply two Hadamard gates on the frequency modes ω_0, ω_1 and ω_4, ω_5. This leverages the possibility to operate in parallel on many qubits. To allow the parallelization of the quantum gates for the whole C-band, it is necessary to compensate for the dispersion in the fiber between the two modulators. To this end, the PF in the middle of the [EOM–PF–EOM] setup applies a supplementary phase shift over the whole PF spectrum corresponding to a negative dispersion of -0.4 ps/nm.

5 Appendix B: Evaluating the Performance for Quantum Key Distribution

We use the coincidences in the $\mathbb{Z}$ basis ($C_{0,0}$, $C_{0,1}$, $C_{1,0}$, $C_{1,1}$) and the $\mathbb{X}$ basis ($C_{+,+}$, $C_{+,-}$, $C_{-,+}$, $C_{-,-}$) to compute the raw coincidence rate, QBER, and sifted key rate. The raw numbers of coincidences in these bases are equal to[34]

$$C_{\mathbb{Z}} = \frac{1}{2}(C_{0,0} + C_{0,1} + C_{1,0} + C_{1,1}), \tag{4}$$

$$C_{\mathbb{X}} = \frac{1}{2}(C_{+,+} + C_{+,-} + C_{-,+} + C_{-,-}). \tag{5}$$

If the integration time is τ, the raw coincidence rate is then

$$R_{\text{raw}} = \frac{1}{2}\frac{C_{\mathbb{Z}} + C_{\mathbb{X}}}{\tau}. \tag{6}$$

The QBER is the ratio of accidental to total coincidences over the two bases,

$$e = \frac{C_{0,1} + C_{1,0} + C_{+,-} + C_{-,+}}{C_{\mathbb{Z}} + C_{\mathbb{X}}}. \tag{7}$$

We compute the sifted key rate using formulas in Ref. 48, accounting for error correction.

Disclosures

The authors declare no conflicts of interest.

Code and Data Availability

The data and code supporting this study are available from the corresponding authors upon request.

Acknowledgments

This work has been supported by Region Ile-de-France in the framework of DIM SIRTEQ. Lorenzo M. Procopio acknowledges the European Union's Horizon 2020 research under the Marie Skłodowska-Curie (Grant No. 800306).

References

1. J. M. Lukens and P. Lougovski, "Frequency-encoded photonic qubits for scalable quantum information processing," *Optica* **4**, 8–16 (2017).
2. M. Kues et al., "On-chip generation of high-dimensional entangled quantum states and their coherent control," *Nature* **546**, 622–626 (2017).
3. P. Imany et al., "50-GHz-spaced comb of high-dimensional frequency-bin entangled photons from an on-chip silicon nitride microresonato," *Opt. Express* **26**, 1825–1840 (2018).
4. H.-H. Lu et al., "Bayesian tomography of high-dimensional on-chip biphoton frequency combs with randomized measurements," *Nat. Commun.* **13**, 4338 (2022).
5. H. Mahmudlu et al., "Fully on-chip photonic turnkey quantum source for entangled qubit/qudit state generation," *Nat. Photonics* **17**, 518–524 (2023).
6. P. Imany et al., "Frequency-domain Hong-Ou-Mandel interference with linear optics," *Opt. Lett.* **43**, 2760–2763 (2018).
7. H.-H. Lu et al., "Quantum interference and correlation control of frequency-bin qubits," *Optica* **5**, 1455–1460 (2018).
8. M. Cabrejo-Ponce et al., "High-dimensional entanglement for quantum communication in the frequency domain," *Laser Photonics Rev.* **17**, 2201010 (2023).
9. M. Clementi et al., "Programmable frequency-bin quantum states in a nano-engineered silicon device," *Nat. Commun.* **14**, 176 (2023).
10. M. Borghi et al., "Reconfigurable silicon photonic chip for the generation of frequency-bin-entangled qudits," *Phys. Rev. Appl.* **19**, 064026 (2023).
11. F. A. Sabattoli et al., "A silicon source of frequency-bin entangled photons," *Opt. Lett.* **47**, 6201–6204 (2022).
12. A. K. Kashi and M. Kues, "Spectral Hong-Ou-Mandel interference between independently generated single photons for scalable frequency-domain quantum processing," *Laser Photonics Rev.* **15**(5), 2000464 (2021).
13. J. Wang et al., "Integrated photonic quantum technologies," *Nat. Photonics* **14**, 273–284 (2020).
14. X. Zhang et al., "Correlated photon pair generation in low-loss double-stripe silicon nitride waveguides," *J. Opt.* **18**, 074016 (2016).
15. F. Samara et al., "High-rate photon pairs and sequential Time-Bin entanglement with Si_3N_4 microring resonators," *Opt. Express* **27**, 19309–19318 (2019).
16. Z. Yin et al., "Frequency correlated photon generation at telecom band using silicon nitride ring cavities," *Opt. Express* **29**, 4821–4829 (2021).
17. S. Clemmen et al., "Continuous wave photon pair generation in silicon-on-insulator waveguides and ring resonators," *Opt. Express* **17**, 16558–16570 (2009).
18. T. Kobayashi et al., "Frequency-domain Hong-Ou-Mandel interference," *Nat. Photonics* **10**, 441–444 (2016).
19. M. G. Raymer et al., "Interference of two photons of different color," *Opt. Commun.* **283**, 747–752 (2010).
20. L. Olislager et al., "Creating and manipulating entangled optical qubits in the frequency domain," *Phys. Rev. A* **89**, 052323 (2014).
21. L. Olislager et al., "Frequency-bin entangled photons," *Phys. Rev. A* **82**, 013804 (2010).
22. M. Bloch et al., "Frequency-coded quantum key distribution," *Opt. Lett.* **32**, 301–303 (2007).
23. H.-H. Lu et al., "Electro-optic frequency beamsplitters and tritters for high-fidelity photonic quantum information processing," *Phys. Rev. Lett.* **120**, 030502 (2018).
24. H.-H. Lu et al., "Fully arbitrary control of frequency-bin qubits," *Phys. Rev. Lett.* **125**, 120503 (2020).
25. H.-H. Lu et al., "A controlled-NOT gate for frequency-bin qubits," *NPJ Quantum Inf.* **5**, 24 (2019).
26. H.-H. Lu et al., "Subatomic many-body physics simulations on a quantum frequency processor," in *Conf. Lasers and Electro-Opt.*, Optical Society of America, p. FTh3A.6 (2019).
27. H.-H. Lu et al., "High-dimensional discrete Fourier transform gates with a quantum frequency processor," *Opt. Express* **30**, 10126–10134 (2022).
28. S. Azzini et al., "From classical four-wave mixing to parametric fluorescence in silicon microring resonators," *Opt. Lett.* **37**, 3807–3809 (2012).
29. T.-Y. Chen et al., "Field test of a practical secure communication network with decoy-state quantum cryptography," *Opt. Express* **17**, 6540–6549 (2009).
30. I. Herbauts et al., "Demonstration of active routing of entanglement in a multi-user network," *Opt. Express* **21**, 29013–29024 (2013).
31. W. Wen et al., "Realizing an entanglement-based multiuser quantum network with integrated photonics," *Phys. Rev. Appl.* **18**, 024059 (2022).
32. Y. Zheng et al., "Multichip multidimensional quantum networks with entanglement retrievability," *Science* **381**(6654), 221–226 (2023).
33. S. Wengerowsky et al., "Entanglement-based wavelength multiplexed quantum communication network," *Nature* **564**, 225–228 (2018).
34. F. Appas et al., "Flexible entanglement-distribution network with an AlGaAs chip for secure communications," *NPJ Quantum Inf.* **7**, 118 (2021).
35. S. K. Joshi et al., "A trusted-node-free eight-user metropolitan quantum communication network," *Sci. Adv.* **6**, eaba0959 (2020).
36. N. B. Lingaraju et al., "Adaptive bandwidth management for entanglement distribution in quantum networks," *Optica* **8**, 329–332 (2021).
37. I. Choi, R. J. Young, and P. D. Townsend, "Quantum information to the home," *New J. Phys.* **13**, 063039 (2011).
38. X. Liu et al., "40-user fully connected entanglement-based quantum key distribution network without trusted node," *PhotoniX* **3**, 2 (2022).
39. F. Boeuf et al., "Silicon photonics R&D and manufacturing on 300-mm wafer platform," *J. Lightwave Technol.* **34**, 286–295 (2016).

40. W. Bogaerts and S. K. Selvaraja, "Compact single-mode silicon hybrid rib/strip waveguide with adiabatic bends," *IEEE Photonics J.* **3**, 422–432 (2011).
41. P. T. Do et al., "Wideband tunable microwave signal generation in a silicon-micro-ring-based optoelectronic oscillator," *Sci. Rep.* **10**, 6982 (2020).
42. F. Mazeas et al., "High-quality photonic entanglement for wavelength-multiplexed quantum communication based on a silicon chip," *Opt. Express* **24**, 28731–28738 (2016).
43. D. Oser et al., "High-quality photonic entanglement out of a standalone silicon chip," *NPJ Quantum Inf.* **6**, 31 (2020).
44. O. Alibart, "Source de photons uniques annoncés à 1550 nm en optique guidée pour les communications quantiques," Theses, Université Nice Sophia Antipolis (2004).
45. W. C. Jiang et al., "Silicon-chip source of bright photon pairs," *Opt. Express* **23**, 20884–20904 (2015).
46. E. Fitzke et al., "Scalable network for simultaneous pairwise quantum key distribution via entanglement-based time-bin coding," *PRX Quantum* **3**, 020341 (2022).
47. O. E. Sandoval et al., "Polarization diversity phase modulator for measuring frequency-bin entanglement of a biphoton frequency comb in a depolarized channel," *Opt. Lett.* **44**, 1674–1677 (2019).
48. C. Autebert et al., "Multi-user quantum key distribution with entangled photons from an AlGaAs chip," *Quantum Sci. Technol.* **6**, 01LT02 (2016).
49. N. Lütkenhaus, "Security against individual attacks for realistic quantum key distribution," *Phys. Rev. A* **61**, 052304 (2000).
50. B. E. Nussbaum et al., "Design methodologies for integrated quantum frequency processors," *J. Lightwave Technol.* **40**, 7648–7657 (2022).
51. Y. Hu et al., "On-chip electro-optic frequency shifters and beam splitters," *Nature* **599**, 587–593 (2021).
52. S. Buddhiraju et al., "Arbitrary linear transformations for photons in the frequency synthetic dimension," *Nat. Commun.* **12**, 2401 (2021).
53. M. He et al., "High-performance hybrid silicon and lithium niobate Mach-Zehnder modulators for 100 Gbit s^{-1} and beyond," *Nat. Photonics* **13**, 359–364 (2019).
54. X. Wang et al., "Integrated thin-silicon passive components for hybrid silicon-lithium niobate photonics," *Opt. Contin.* **6**, 2233–2244 (2022).
55. F. Valdez et al., "110 GHz, 110 mW hybrid silicon-lithium niobate Mach-Zehnder modulator," *Sci. Rep.* **12**, 18611 (2022).

Antoine Henry received his PhD in quantum optics from the Institut Polytechnique de Paris, supervised by Prof. Isabelle Zaquine at Telecom Paris and Dr. Nadia Belabas at the Centre for Nanosciences and Nanotechnology (C2N). His research focuses on generating quantum states of light at telecom wavelengths using integrated structures. He investigated the manipulation of quantum states in the frequency domain and their applications to quantum communication.

Dario A. Fioretto did his PhD work in Innsbruck on experimental quantum network schemes based on trapped ions, supervised by Prof. Northup. He continued his academic career at C2N, where he joined as a postdoc in the quantum dot group of Prof. Pascale Senellart working on deterministic cluster states generation and where he is now working as a researcher between C2N and Quandela.

Lorenzo M. Procopio received his PhD in physics from the University of Vienna in 2017. He was a postdoctoral researcher at the Centre for Nanosciences and Nanotechnology in France and Weizmann Institute of Science in Israel, from 2017 to 2020 and from 2020 to 2024, respectively. He is currently a Senior Postdoc at the University Paderborn. His research interests include the fields of photonic quantum information, quantum optics, and nonlinear optics.

Stéphane Monfray is currently a principal engineer with STMicroelectronics and an expert in advanced technologies. He is also the author or coauthor of more than 130 publications and received the Grand Prix of electronics General Ferrié in 2012. He has over 10 years of experience on advanced CMOS technologies.

Frédéric Boeuf obtained his MEng and MSc degrees from the Institut National Polytechnique de Grenoble in 1996 and PhD in condensed matter physics from the University of Grenoble in 2000. Then, he joined STMicroelectronics in working on advanced devices physics and integration. He's currently regional fellow and photonics innovation technical director inside STMicroelectonics' Technology and Design Platform Organization.

Eric Cassan has been a professor at Université Paris-Saclay since 2009 and a researcher at C2N (Centre de Nanosciences et de Nanotechnologies CNRS/UPSaclay). His field is integrated photonics, more specifically silicon photonics, where he works within the team and with students on the development of components/structures/circuits exploiting nonlinear optical effects and the engineering of diffractive and non-diffractive structures in integrated optics based on the integration of active materials compatible with the silicon processes.

Carlos Alonso Ramos is a researcher at the Center for Nanoscience and Nanotechnology, France. His research activities focus on the study of fundamental concepts for the development of high-performance photonic devices. He has been at the forefront of the development of passive silicon photonic devices and has recently made key demonstrations of nonlinear and optomechanical interactions in silicon. He is co-author of more than 100 papers and has delivered over 40 invited presentations.

Laurent Vivien is a CNRS director of Research at the Centre for Nanoscience and Nanotechnology, expert on the development of fundamental concepts for silicon photonics including optoelectronic and hybrid photonic devices for a large range of applications including optical communications, sensing, and quantum. He also received his Consolidator ERC grant on strained silicon photonics in 2015, and in 2023, the Advanced ERC grant on the hybrid integration of doped crystalline oxides in silicon photonics. He is also an elected fellow of OPTICA, SPIE, and EOS.

Kamel Bencheikh obtained his PhD in physics in 1996. After a postdoctoral position as an Alexander Von-Humboldt fellow at the University of Konstanz in Germany, he joined in 1999 the CNRS as a full-time researcher, working at the Center of Nanoscience and Nanotechnology. His main activities are dedicated to nonlinear optics, quantum optics, and nanophotonics.

Isabelle Zaquine obtained her PhD in 1985 from the University of Grenoble. At first, she was a research engineer at Thales Research and Technology and finally a professor at Télécom Paris, part of the Institut Polytechnique de Paris and was head of the group Quantum Information and Applications. Her main interests were on entangled photon pair sources for quantum communications with an emphasis on the use of standard telecom devices and lately on the frequency degree of freedom.

Nadia Belabas has been a CNRS researcher since 2004. She is an expert in semiconductor nanophotonics and quantum optics. She initially worked on broadband pulse-shaping, Fourier transform, and multidimensional spectroscopy. She then notably opened prospects in classical and quantum photonics with innovative and controlled guided light manipulation and sources. Her current interest lies in implementing quantum tasks with semiconductors sources and beyond, both in the continuous and discrete variable framework.